

# Active Diffusion Subsampling

Oisín Nolan, Tristan S. W. Stevens, Wessel L. van Nierop, Ruud J. G. van Sloun  
Eindhoven University of Technology  
{o.i.nolan, t.s.w.stevens, w.l.v.nierop, r.j.g.v.sloun}@tue.nl

## Abstract

Subsampling is commonly used to mitigate costs associated with data acquisition, such as time or energy requirements, motivating the development of algorithms for estimating the fully-sampled signal of interest  $\mathbf{x}$  from partially observed measurements  $\mathbf{y}$ . In maximum-entropy sampling, one selects measurement locations that are expected to have the highest entropy, so as to minimize uncertainty about  $\mathbf{x}$ . This approach relies on an accurate model of the posterior distribution over future measurements, given the measurements observed so far. Recently, diffusion models have been shown to produce high-quality posterior samples of high-dimensional signals using *guided diffusion*. In this work, we propose *Active Diffusion Subsampling* (ADS), a method for performing active subsampling using guided diffusion in which the model tracks a distribution of beliefs over the true state of  $\mathbf{x}$  throughout the reverse diffusion process, progressively decreasing its uncertainty by choosing to acquire measurements with maximum expected entropy, and ultimately generating the posterior distribution  $p(\mathbf{x} | \mathbf{y})$ . ADS can be applied using pre-trained diffusion models for any subsampling rate, and does not require task-specific retraining – just the specification of a measurement model. Furthermore, the maximum entropy sampling policy employed by ADS is interpretable, enhancing transparency relative to existing methods using black-box policies. Experimentally, we show that ADS outperforms fixed sampling strategies, and study an application of ADS in Magnetic Resonance Imaging acceleration using the fastMRI dataset, finding that ADS performs competitively with supervised methods. Code available at <https://active-diffusion-subsampling.github.io/>.

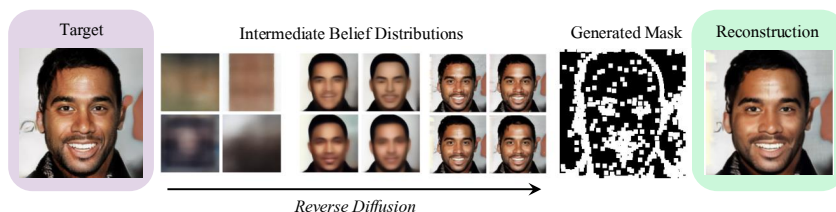


Figure 1: *Active Diffusion Subsampling* jointly designs a subsampling mask and reconstructs the target signal in a single reverse diffusion process.

## 1 Introduction

In recent years, diffusion models have defined the state of the art in inverse problem solving, particularly in the image domain, through novel posterior sampling methods such as *Diffusion Posterior Sampling* (DPS) (Chung et al., 2022) and *Posterior Sampling with Latent Diffuion* (PSLD) (Rout et al., 2024). These methods are often evaluated on inverse imaging problems, such as inpainting, which is akin to image subsampling. Typical benchmarks evaluate inpainting ability using

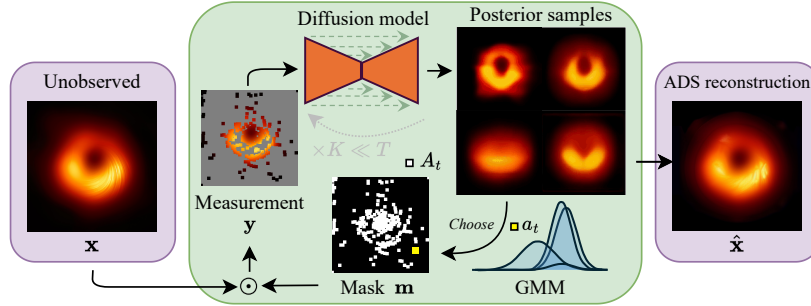


Figure 2: Schematic overview of the proposed Active Diffusion Sampling (ADS) method.

naïve subsampling masks such as randomly masked pixels, or a box mask in the center of the image (Rout et al., 2024). In real-world applications, however, more sophisticated subsampling strategies are typically employed, for example, in Magnetic Resonance Imaging (MRI) acceleration (Lustig and Pauly, 2010; Bridson, 2007). These subsampling strategies are usually designed by domain experts, and are therefore not generalizable across tasks. Some recent literature has explored learning subsampling masks for various tasks (Bahadir et al., 2020; Baldassarre et al., 2016; Huijben et al., 2020; Van Gorp et al., 2021), but these methods typically depend on black-box policy functions, and require task-specific training. In this work, we introduce *Active Diffusion Sampling* (ADS), an algorithm for automatically designing task- and sample-adaptive subsampling masks using diffusion models, without the need for further training or fine-tuning (Figure 2). ADS uses a white-box policy function based on maximum entropy sampling (Caticha, 2021), in which the model chooses sampling locations that are expected to maximize the information gained about the reconstruction target. In order to implement this policy, ADS leverages quantities that are already computed during the reverse diffusion process, leading to minimal additional computation. Our main contributions are thus as follows:

- A novel approach to active subsampling which can be employed with existing diffusion models using popular posterior sampling methods;
- A white-box policy function for sample selection, grounded in theory from Bayesian experimental design;
- Experimental validation against baseline sampling strategies and via application to MRI acceleration.

## 2 Related Work

Methods aiming to select maximally informative measurements appear in many domains, spanning statistics, signal processing, and machine learning, but sharing foundations in information theory and Bayesian inference. Optimal Bayesian Experimental Design (Lindley, 1956) aims to determine which experiment will be most informative about some quantity of interest  $\theta$  (Rainforth et al., 2024), typically parameters of a statistical model. Active learning (Houlsby et al., 2011) performs an analogous task in machine learning, aiming to identify which samples, if included in the training set, would lead to the greatest performance gain on the true data distribution. While our method focuses on subsampling high-dimensional signals, it could also be interpreted as a Bayesian regression solver for the forward problem  $\mathbf{y} = f(\mathbf{x}) + \mathbf{n}$ , in which  $\mathbf{x}$  is now seen as parameters for a model  $f$ , and the active sampler seeks measurements  $\mathbf{y}$  which minimize uncertainty about the parameters  $\mathbf{x}$ , as in Bayesian experimental design.

A popular approach to subsampling from signal processing is compressive sensing, in which sparse signals are reconstructed from measurements with sub-Nyquist sampling rates (Rani et al., 2018), and typically applied in imaging and communication. Measurement matrices relating observed measurements to the signal of interest  $\mathbf{x}$  are then designed so as to minimize reconstruction error on  $\mathbf{x}$ . In Bayesian compressive sensing, measurement matrices are designed so as to minimize a measure of uncertainty about the value of  $\mathbf{x}$ . Adaptive approaches, such as that of Braun et al. (2015), aim to decrease this uncertainty iteratively, by greedily choosing measurements that maximise the mutual

information between  $\mathbf{x}$  and  $\mathbf{y} = \mathbf{U}\mathbf{x} + \mathbf{n}$ . These methods typically assume a Gaussian prior on  $\mathbf{x}$ , however, limiting the degree to which more complex prior structure can be used.

More recently, a number of methods using deep learning to design subsampling strategies have emerged. These approaches typically learn subsampling strategies from data that minimize reconstruction error between  $\mathbf{x}$  and  $\mathbf{y}$ . Methods by Huijben et al. (2020) and Bahadir et al. (2020) learn fixed sampling strategies, in which a single mask is designed *a priori* for a given domain, and applied to all samples for inference. These methods can be effective, but suffer in cases where optimal masks differ across samples. Sample-adaptive methods (Van Gorp et al., 2021; Bakker et al., 2020; Yin et al., 2021; Stevens et al., 2022) move past this limitation by designing sampling strategies at inference time. A popular application of such methods is MRI acceleration, spurred by the fastMRI benchmark (Zbontar et al., 2018), in which a full MRI image must be reconstructed from sub-sampled  $\kappa$ -space measurements. In A-DPS (Van Gorp et al., 2021), for example, a neural network is trained to build an acquisition mask consisting of  $M$   $\kappa$ -space lines iteratively, adaptively adding new lines based on the current reconstruction and prior context. Bakker et al. (2020) implements the same procedure using a reinforcement learning agent. One drawback of these methods is their reliance on black-box policies, making it difficult to detect and interpret failure cases. Generative approaches with transparent sampling policies circumvent this issue. For example, CLUDAS (Sanchez et al., 2020) is a generative approach to adaptive MRI acquisition design, using a conditional Wasserstein GAN to generate posterior samples over MRI image, and maximum-variance sampling in the  $\kappa$ -space as the measurement selection policy. The performance of generative approaches such as CLUDAS depends on how well they can model the true posterior distribution over  $\mathbf{x}$  given observations. For this reason, ADS is designed to leverage state-of-the-art posterior sampling methods enabled by diffusion models, such as Posterior Sampling with Latent Diffusion (Rout et al., 2024). Furthermore, Diffusion Models have shown excellent performance in diverse domain, such as computer vision Dhariwal and Nichol (2021), medical imaging (Chung and Ye, 2022; Stevens et al., 2024), and natural language processing (Yu et al., 2022), and more, enhancing the potential for generalizability.

### 3 Background

#### 3.1 Bayesian Optimal Experimental Design

In Bayesian Optimal Experimental Design (Rainforth et al., 2024) and Bayesian Active Learning (Houlsby et al., 2011), the objective is to choose the optimal *design*, or set of actions  $A = A^*$ , leading to new observations of a measurement variable  $\mathbf{y}$  that will minimise uncertainty about a related quantity of interest  $\mathbf{x}$ , as measured by entropy  $H$ . It was shown by Lindley (1956) that this objective is equivalent to finding the actions  $A$  that maximise the mutual information  $I$  between  $\mathbf{x}$  and  $\mathbf{y}$ , i.e. selecting actions leading to observations of  $\mathbf{y}$  that will be most informative about  $\mathbf{x}$ :

$$A^* = \arg \min_A [H(\mathbf{x} | A, \mathbf{y})] = \arg \max_A [I(\mathbf{y}; \mathbf{x} | A)] \quad (1)$$

This objective is commonly optimized *actively*, wherein the design is created iteratively by choosing actions that maximise mutual information, considering past observations when selecting new actions (Rainforth et al., 2024). This active paradigm invites an agent-based framing, in which the agent’s goal is to minimize its own uncertainty, and beliefs over  $\mathbf{x}$  are updated as new measurements of  $\mathbf{y}$  are taken. The active design objective can be formulated as follows, where  $a_t$  is possible action at time  $t$ ,  $A_t = A_{t-1} \cup a_t$  is the set of actions  $\{a_0, \dots, a_t\}$  taken so far at time  $t$ , and  $\mathbf{y}_{t-1}$  is the set of partial observations of the measurement variable  $\mathbf{y}$  until time  $t - 1$ :

$$\begin{aligned} a_t^* &= \arg \max_{a_t} [I(\mathbf{y}_t; \mathbf{x} | A_t, \mathbf{y}_{t-1})] \\ &= \arg \max_{a_t} [\mathbb{E}_{p(\mathbf{y}_t | \mathbf{x}, A_t) p(\mathbf{x} | \mathbf{y}_{t-1})} [\log p(\mathbf{y}_t | A_t, \mathbf{y}_{t-1}) - \log p(\mathbf{y}_t | \mathbf{x}, A_t, \mathbf{y}_{t-1})]] \\ &= \arg \max_{a_t} [H(\mathbf{y}_t | A_t, \mathbf{y}_{t-1}) - H(\mathbf{y}_t | \mathbf{x}, A_t, \mathbf{y}_{t-1})] \end{aligned} \quad (2)$$

We can interpret the agent’s behaviour from Equation 2 as trying to maximise marginal uncertainty about  $\mathbf{y}_t$ , while minimising model uncertainty about what value  $\mathbf{y}_t$  should take on given a particular  $\mathbf{x}$  (Houlsby et al., 2011). Active designs are typically preferred over *fixed* designs, in which a set of actions is chosen up-front, as opposed to being chosen progressively as measurements are acquired

(Rainforth et al., 2024). While fixed designs may be more computationally efficient, they are less sample-specific, which can lead to lower information gain about  $\mathbf{x}$ . Finally, it is worth noting that this active optimization scheme, while greedy, has been shown to be near-optimal due to the submodularity of conditional entropy (Golovin and Krause, 2011).

### 3.2 Subsampling

Generally image reconstruction tasks can be formulated as inverse problems, given by:

$$\mathbf{y} = \mathbf{U}\mathbf{x} + \mathbf{n}, \quad (3)$$

where  $\mathbf{y} \in \mathcal{Y}^M$  is a measurement,  $\mathbf{x} \in \mathcal{X}^N$  the signal of interest and  $\mathbf{n} \in \mathcal{N}^M$  some noise source, typically Gaussian. For the subsampling problem, the measurement matrix  $\mathbf{U} \in \mathbb{R}^{M \times N}$  can be expressed in terms of a binary subsampling matrix using one-hot encoded rows such that we have an element-wise mask  $\mathbf{m} = \text{diag}(\mathbf{U}^\top \mathbf{U})$ , where only the diagonal entries of  $\mathbf{U}^\top \mathbf{U}$  are retained, representing the subsampling pattern. We can relate the subsampling mask  $\mathbf{m}$  through the zero-filled measurement which can be obtained through  $\mathbf{y}_{zf} = \mathbf{U}^\top \mathbf{y} = \mathbf{m} \odot \mathbf{x} + \mathbf{U}^\top \mathbf{n}$ .

Since we are interested in the adaptive design of these masks, we formulate their generation by  $\mathbf{m} = \mathbf{U}(A_t)^\top \mathbf{U}(A_t)$ , where the measurement matrix is now a function of the actions  $A_t = \{a_0, \dots, a_t\}$  taken by the agent up to time  $t$ . The  $i^{\text{th}}$  element of that mask is defined as follows:

$$\mathbf{m} = [\mathbf{U}(A_t)^\top \mathbf{U}(A_t)]_i = \begin{cases} 1 & \text{if } i \in A_t \\ 0 & \text{otherwise.} \end{cases} \quad (4)$$

The measurement model in (3) can now be extended to an active setting via  $\mathbf{y}_t = \mathbf{U}(A_t)\mathbf{x} + \mathbf{n}_t$ . Note too that in some applications we have an additional *forward model*  $f$ , mapping from the data domain to the measurement domain, yielding  $\mathbf{y}_t = \mathbf{U}(A_t)f(\mathbf{x}) + \mathbf{n}_t$ .

### 3.3 Posterior Sampling with Diffusion Models

Denoising diffusion models learn to reverse a stochastic differential equation (SDE) that progressively noises samples  $\mathbf{x}$  towards a standard Normal distribution Song et al. (2020b). The SDE defining the noising process is as follows:

$$d\mathbf{x} = -\frac{\beta(\tau)}{2}\mathbf{x}d\tau + \sqrt{\beta(\tau)}d\mathbf{w} \quad (5)$$

where  $\mathbf{x}(0) \in \mathbb{R}^d$  is an initial clean sample,  $\tau \in [0, T]$ ,  $\beta(\tau)$  is the noise schedule, and  $w$  is a standard Wiener process, and  $\mathbf{x}(T) \sim \mathcal{N}(0, I)$ . According the following equation from Anderson (1982), this SDE can be reversed once the score function  $\nabla_{\mathbf{x}} \log p_\tau(\mathbf{x})$  is known, where  $\bar{w}$  is a standard Wiener process running backwards:

$$d\mathbf{x} = \left[ -\frac{\beta(\tau)}{2}\mathbf{x} - \beta(\tau)\nabla_{\mathbf{x}} \log p_\tau(\mathbf{x}) \right] d\tau + \sqrt{\beta(\tau)}d\bar{\mathbf{w}} \quad (6)$$

Following the notation by Ho et al. (2020) and Chung et al. (2022), the discrete setting of the SDE is represented using  $x_\tau = \mathbf{x}(\tau T/N)$ ,  $\beta_\tau = \beta(\tau T/N)$ ,  $\alpha_\tau = 1 - \beta_\tau$ ,  $\bar{\alpha}_\tau = \prod_{s=1}^{\tau} \alpha_s$ , where  $N$  is the numbers of discretized segments. The diffusion model achieves the SDE reversal by learning the score function using a neural network parameterised by  $\theta$ ,  $s_\theta(\mathbf{x}_\tau, \tau) \simeq \nabla_{\mathbf{x}_\tau} \log p_\tau(\mathbf{x}_\tau)$ .

The reverse diffusion process can be conditioned on a measurement  $\mathbf{y}$  to produce samples from the posterior  $p(\mathbf{x}|\mathbf{y})$ . This can be done with substitution of the *conditional score function*  $\nabla_{\mathbf{x}_\tau} \log p_\tau(\mathbf{x}_\tau)$  in (6). The intractability of the noise-perturbed likelihood  $\nabla_{\mathbf{x}_\tau} \log p_\tau(\mathbf{y}|\mathbf{x}_\tau)$  which follows from refactoring the posterior using Bayes' rule has led to various approximate guidance schemes to compute these gradients with respect to a partially-noised sample  $\mathbf{x}_\tau$  (Chung et al., 2022; Song et al., 2023; Rout et al., 2024). Most of these rely on Tweedie's formula, which can be thought of as a one-step denoising process from  $\tau \rightarrow 0$ , denoted  $\mathcal{D}_\tau(\cdot)$ , using our trained diffusion model to estimate the true fully-denoised sample  $\mathbf{x}_0$  as follows:

$$\hat{\mathbf{x}}_0 = \mathbb{E}[\mathbf{x}_0|\mathbf{x}_\tau] = \mathcal{D}_\tau(\mathbf{x}_\tau) = \frac{1}{\sqrt{\bar{\alpha}_\tau}}(\mathbf{x}_\tau + (1 - \bar{\alpha}_\tau)s_\theta(\mathbf{x}_\tau, \tau). \quad (7)$$

*Diffusion Posterior Sampling* (DPS) uses (7) to approximate  $\nabla_{\mathbf{x}_\tau} \log p(\mathbf{y}|\mathbf{x}_\tau) \approx \nabla_{\mathbf{x}_\tau} \log p(\mathbf{y}|\hat{\mathbf{x}}_0)$ . In the case of active subsampling, this leads to guidance term  $\nabla_{\mathbf{x}_\tau} \|\mathbf{y}_t - U(A_t)f(\hat{\mathbf{x}}_0)\|_2^2$  indicating

the direction in which  $x_\tau$  should step in order to be more consistent with  $\mathbf{y}_t = U(A_t)f(\mathbf{x}) + \mathbf{n}$ . The conditional reverse diffusion process then alternates between standard reverse diffusion steps and guidance steps in order to generate samples from the posterior  $p(\mathbf{x} | \mathbf{y}_t)$ .

## 4 Method

### 4.1 Active Diffusion Subsampling

---

#### Algorithm 1: Active Diffusion Subsampling

---

**Require:**  $T, N_p, S, \zeta, \{\tilde{\sigma}_\tau\}_{\tau=0}^T, \{\alpha_\tau\}_{\tau=0}^T, A_{\text{init}}$

- 1  $t = 0$ ;  $A_0 = A_{\text{init}}$ ;  $\mathbf{y}_0 = \mathbf{U}(A_0)f(\mathbf{x}) + \mathbf{n}_0$ ;  $\{\mathbf{x}_T^{(i)} \sim \mathcal{N}(\mathbf{0}, \mathbf{I})\}_{i=0}^{N_p-1}$
- 2 **for**  $\tau = T$  **to** 1 **do**
- 3     **for**  $i = 0$  **to**  $N_p - 1$  **do**
- 4          $\hat{\mathbf{s}} \leftarrow \mathbf{s}_\theta(\mathbf{x}_\tau^{(i)}, \tau)$
- 5          $\hat{\mathbf{x}}_0^{(i)} \leftarrow \mathcal{D}_\tau(\mathbf{x}_\tau^{(i)}) = \frac{1}{\sqrt{\alpha_\tau}}(\mathbf{x}_\tau^{(i)} + (1 - \alpha_\tau)\hat{\mathbf{s}})$
- 6          $\hat{\mathbf{y}}^{(i)} \leftarrow f(\hat{\mathbf{x}}_0^{(i)})$  // Estimate the full measurement
- 7          $\mathbf{z} \sim \mathcal{N}(\mathbf{0}, \mathbf{I})$
- 8          $\mathbf{x}_{\tau-1}^{(i)'} \leftarrow \frac{\sqrt{\alpha_\tau(1-\alpha_{\tau-1})}}{1-\alpha_\tau}\mathbf{x}_\tau^{(i)} + \frac{\sqrt{\alpha_{\tau-1}\beta_\tau}}{1-\alpha_\tau}\hat{\mathbf{x}}_0^{(i)} + \tilde{\sigma}_\tau\mathbf{z}$
- 9          $\mathbf{x}_{\tau-1}^{(i)} \leftarrow \mathbf{x}_{\tau-1}^{(i)'} - \zeta \nabla_{\mathbf{x}_\tau^{(i)}} \|\mathbf{y}_t - \mathbf{U}(A_t)\hat{\mathbf{y}}^{(i)}\|_2^2$
- 10     **if**  $\tau \in S$  **then**
- 11          $t \leftarrow t + 1$
- 12          $a_t^* = \arg \max_{a_t} \left[ \sum_i \log \sum_j \exp \left\{ \frac{\sum_{l \in a_t} (\hat{\mathbf{y}}_l^{(i)} - \hat{\mathbf{y}}_l^{(j)})^2}{2\sigma_y^2} \right\} \right]$
- 13          $A_t = A_{t-1} \cup a_t^*$
- 14          $\mathbf{y}_t = \mathbf{U}(A_t)f(\mathbf{x}) + \mathbf{n}_t$  // Acquire new measurements
- 15     **end**

**return:**  $\hat{\mathbf{x}}_0 = \frac{1}{N_p} \sum_i \hat{\mathbf{x}}_0^{(i)}$  // Return the posterior mean

---

ADS operates by running a reverse diffusion process for a batch  $\{\mathbf{x}_\tau^{(i)}\}, i \in 0, \dots, N_p$  guided by an evolving set of measurements  $\{\mathbf{y}_t\}_{t=0}^T$  which are revealed to it through subsampling actions taken at reverse diffusion steps satisfying  $\tau \in S$ , where  $S$  is a subsampling schedule. We refer to the elements of this batch  $\{\mathbf{x}_\tau^{(i)}\}$  as *particles* in the data space, as they implicitly track a belief distribution over the true, fully-denoised  $\mathbf{x} = \mathbf{x}_0$  throughout reverse diffusion. These particles are used to compute estimates of uncertainty about  $\mathbf{x}$ , which ADS aims to minimize by choosing actions  $a_t$  that maximize the mutual information between  $\mathbf{x}$  and  $\mathbf{y}_t$  given  $a_t$ , as explained in Section 3.1. The remainder of the section describes how this is achieved through (i) employing running estimates of  $\mathbf{x}_0$  given by  $\mathcal{D}_\tau(\mathbf{x}_\tau)$ , (ii) modelling assumptions on the measurement entropy, and (iii) computational advantages afforded by the subsampling operator.

ADS follows an information-maximizing policy, selecting measurements  $a_t^* = \arg \max_{a_t} [I(\mathbf{y}; \mathbf{x} | A_t, \mathbf{y}_{t-1})]$ . Assuming a measurement model with additive noise  $\mathbf{y}_t = \mathbf{U}(A_t)f(\mathbf{x}) + \mathbf{n}_t$ , the posterior entropy term  $H(\mathbf{y}_t | \mathbf{x}, A_t, \mathbf{y}_{t-1})$  in the mutual information is unaffected by the choice of action  $a_t$ : it is solely determined by the noise component  $\mathbf{n}_t$ . This simplifies the policy function, leaving only the marginal entropy term  $H(\mathbf{y}_t | A_t, \mathbf{y}_{t-1})$  to maximize. This entropy term (Equation 2) can be computed as an expectation of  $\log p(\mathbf{y}_t | A_t, \mathbf{y}_{t-1})$ , or the expected distribution of measurements  $\mathbf{y}_t$  given the observations so far, and a subsampling matrix  $A_t$ . We model these probability distributions in Equation 8 as mixtures of  $N_p$  isotropic Gaussians, with means set as estimates of future measurements under possible actions, and variance  $\sigma_y^2 \mathbf{I}$ . The means  $\hat{\mathbf{y}}_t^{(i)} = \mathbf{U}(A_t)f(\hat{\mathbf{x}}_0^{(i)})$  are computed by applying the forward model to posterior samples  $\hat{\mathbf{x}}_0^{(i)} \sim p(\mathbf{x} | \mathbf{y}_{t-1})$ , which are estimated using the batch of partially denoised particles  $\mathbf{x}_\tau^{(i)}$  via  $\hat{\mathbf{x}}_0^{(i)} = \mathcal{D}_\tau(\mathbf{x}_\tau^{(i)})$ , yielding the GMM:

$$p(\mathbf{y}_t | A_t, \mathbf{y}_{t-1}) = \sum_{i=0}^{N_p-1} \mathbf{w}_i \mathcal{N}(\hat{\mathbf{y}}_t^{(i)}, \sigma_y^2 \mathbf{I}) \quad (8)$$

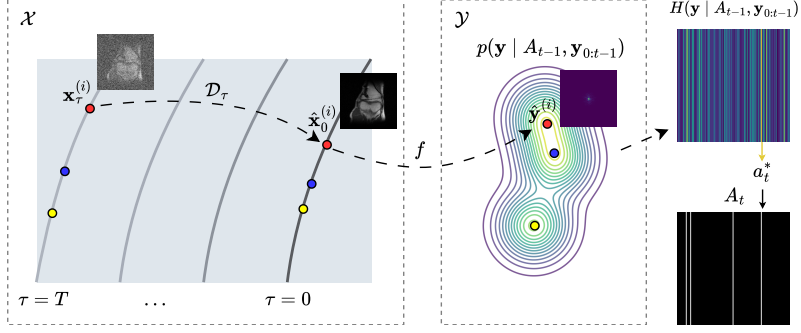


Figure 3: Illustration of a single action selection based on a set of partially-denised particles  $\{\mathbf{x}_\tau^{(i)}\}$ .

Under this isotropic Gaussian Mixture Model, the marginal entropy can be approximated as follows, as given by Hershey and Olsen (2007):

$$H(\mathbf{y}_t | A_t, \hat{\mathbf{y}}_{0:t-1}) \approx \text{constant} + \sum_i^{N_p} w_i \log \sum_j^{N_p} w_j \exp \left\{ \frac{\|\hat{\mathbf{y}}_t^{(i)} - \hat{\mathbf{y}}_t^{(j)}\|_2^2}{2\sigma_y^2} \right\} \quad (9)$$

Finally, we leverage the fact that  $\mathbf{U}(A_t)$  is a subsampling matrix to derive an efficient final formulation of our policy. Because  $\mathbf{U}(A_t)$  is a subsampling matrix, the optimal choice for the next action  $a_t$  will be at the region of the measurement space with the largest disagreement among the particles, as measured by Gaussian error in Equation 9. Therefore, rather than computing a separate set of subsampled particles for each possible next subsampling mask, we instead compute a single set of fully-sampled measurement particles  $\hat{\mathbf{y}}^{(i)} = f(\hat{\mathbf{x}}_0^{(i)})$ , and simply choose the optimal action as the region with largest error. For example, when pixel-subsampling an image, the particles  $\hat{\mathbf{y}}^{(i)}$  become predicted estimates of the full image, given the pixels observed so far, and the next sample is chosen as whichever pixel has the largest total error across the particles. Similarly, in accelerated MRI, the next  $\kappa$ -space line selected is the one in which there is the largest error across estimates of the full  $\kappa$ -space. Denoting as  $l \in a_t$  the set of indices sampled by each possible action  $a_t$ , and assuming equal weights for all particles,  $w_i = w_j, \forall i, j$ , the final form of the policy function is given as follows (see Appendix A.1 for derivation):

$$a_t^* = \arg \max_{a_t} \left[ \sum_i^{N_p} \log \sum_j^{N_p} \exp \left\{ \frac{\sum_{l \in a_t} (\hat{\mathbf{y}}_l^{(i)} - \hat{\mathbf{y}}_l^{(j)})^2}{2\sigma_y^2} \right\} \right] \quad (10)$$

This can be further simplified for element-wise subsampling, in which  $a_t$  represents just a single index, and the squared L2 norm simplifies to a squared error. In this case, denoting as  $\mathcal{E}_{i,j}$  the element-wise Gaussian error matrix between particles  $\hat{\mathbf{y}}^{(i)}$  and  $\hat{\mathbf{y}}^{(j)}$ , we can compute the policy as follows:

$$\mathcal{E}_{i,j} = \exp \left\{ \frac{(\hat{\mathbf{y}}^{(i)} - \hat{\mathbf{y}}^{(j)})^2}{2\sigma_y^2} \right\}; \quad \mathcal{E} = \sum_i^{N_p} \log \sum_j^{N_p} \mathcal{E}_{i,j}; \quad a_t^* = \arg \max_{a_t} \mathcal{E}[a_t] \quad (11)$$

Where the  $[a_t]$  operator selects elements indexed by  $a_t$  from matrix  $\mathcal{E}$ .

## 4.2 Extension of ADS to Latent Diffusion Models

Current state-of-the-art diffusion models are gravitating towards a latent design, which has proven to work effectively on high resolution image synthesis (Rombach et al., 2022) and inversion (Rout et al., 2024). *Latent diffusion models* (LDMs) involve a two-stage training process. First an autoencoder is trained such that  $\hat{\mathbf{x}} = D(\mathbf{z}) = D(E(\mathbf{x}))$ , with encoder  $E$ , decoder  $D$  and  $\mathbf{z}$  denoting the latent variable. Projecting the data into a latent space allows more effective and computationally efficient training in the semantically compressed space. Similarly, by leveraging LDMs, ADS can be scaled to unlock new domains requiring higher resolution. Recently, guidance methods similar to (7)

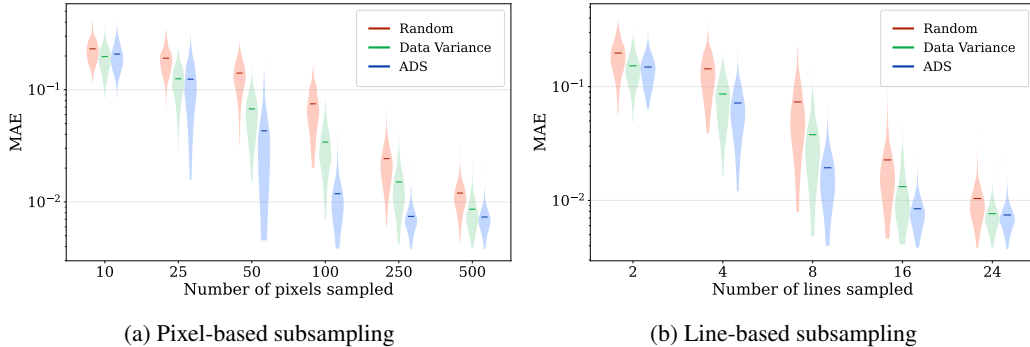


Figure 4: Comparison of ADS (ours) with two non-adaptive baselines. Evaluated based on reconstruction Mean Absolute Error (MAE) on  $N = 500$  unseen samples from the MNIST test set. Note that MAE is plotted on a log scale.

have been extended for LDMs (Rout et al., 2024, 2023). We here show that ADS too can be straightforwardly extended with LDMs using existing guidance methods: estimates of fully sampled measurement particles  $\hat{\mathbf{y}}^{(i)}$  are now computed by first decoding latent variables to the data-space i.e.  $p(\hat{\mathbf{y}}^{(i)}|\hat{\mathbf{x}}_0 = D([\mathbf{z}_0|\mathbf{z}_\tau]))$ . We include several examples using a pretrained Stable Diffusion (Rombach et al., 2022) model out-of-the-box in Appendix A.5 to demonstrate this.

## 5 Experiments

### 5.1 Evaluation of Subsampling Strategies

In order to evaluate the effectiveness of the Maximum Entropy subsampling strategy employed by ADS, we compare it to two baseline subsampling strategies on the task of reconstructing images of digits from the MNIST dataset LeCun et al. (1998). To this end, a Denoising Diffusion Implicit Model (DDIM) Song et al. (2020a) was trained on the MNIST training dataset, resized to  $32 \times 32$  pixels. See Appendix A.2.1 for further details on training and architecture. Using this trained DDIM, each subsampling strategy was used to reconstruct 500 unseen samples from the MNIST test set for various subsampling rates. Both pixel-based and line-based subsampling were evaluated, where line-based subsampling selects single-pixel-wide columns. The measurement model is thus  $\mathbf{y}_t = \mathbf{U}(A_t)\mathbf{x}$ , as there is no measurement noise or measurement transformation, i.e.  $f(\mathbf{x}) = \mathbf{x}$ . The baseline subsampling strategies used for comparison were (i) *Random* subsampling selects measurement locations from a uniform categorical distribution without replacement, and (ii) *Data Variance* subsampling selects measurement locations without replacement from a categorical distribution in which the probability of a given location is proportional to the variance across that location in the training set, leading to a data-driven but fixed design strategy. Inference was performed using Diffusion Posterior Sampling for measurement guidance, with guidance weight  $\zeta = 1$  and  $T = 1000$  reverse diffusion steps. For ADS, measurements were taken at regular intervals in the window  $[0, 800]$ , with 16 particles. For the fixed sampling strategies, the subsampling masks were set *a priori*, such that all diffusion steps are guided by the measurements, as is typical in inverse problem solving with diffusion models. The results to this comparison are given in Table 1, and illustrated by Figure 4. It is clear from these results that ADS outperforms fixed mask baselines, most notably in comparison with data-variance sampling: for pixel-based sampling, we find that maximum entropy sampling with a budget of 100 pixels outperforms data variance sampling with a budget of 250 pixels, i.e. actively sampling the measurements is as good as having  $2.5 \times$  the number of measurements with the data-variance strategy. We also find that the standard deviation of the reconstruction errors over the test set is significantly lower for 25% and 50% subsampling rates (typically  $\sim 2\text{-}3 \times$  than baselines, leading to more reliable reconstructions). In aggregate, these results motivate the use of ADS in applications in which naive or fixed subsampling strategies are being used for inverse problem solving with diffusion models.

No. Pixels Sampled (% of total)	Random	Data Variance	ADS (Ours)
10 (0.97%)	0.231 (0.052)	<b>0.197</b> (0.048)	0.207 (0.054)
25 (2.44%)	0.190 (0.048)	0.125 (0.037)	<b>0.124</b> (0.055)
50 (4.88%)	0.140 (0.041)	0.067 (0.026)	<b>0.042</b> (0.030)
100 (9.76%)	0.074 (0.029)	0.034 (0.014)	<b>0.011</b> (0.005)
250 (24.41%)	0.024 (0.009)	0.015 (0.006)	<b>0.007</b> (0.002)
500 (48.82%)	0.011 (0.003)	0.008 (0.003)	<b>0.007</b> (0.002)
No. Lines Sampled (% of total)	Random	Data Variance	ADS (Ours)
2 (6.25%)	0.197 (0.059)	0.152 (0.045)	<b>0.148</b> (0.042)
4 (12.5%)	0.143 (0.054)	0.086 (0.034)	<b>0.071</b> (0.033)
8 (25%)	0.073 (0.033)	0.037 (0.021)	<b>0.019</b> (0.009)
16 (50%)	0.022 (0.014)	0.013 (0.007)	<b>0.008</b> (0.003)
24 (75%)	0.010 (0.004)	0.0076 (0.0025)	<b>0.0074</b> (0.0023)

Table 1: Mean and (standard deviation) for the Mean Absolute Error ( $\downarrow$ ) in reconstruction of MNIST samples, using pixel- and line-based subsampling.

## 5.2 Application in MRI Acceleration

To assess the real-world practicability of ADS, it was evaluated on the popular fastMRI (Zbontar et al., 2018)  $4\times$  acceleration benchmark for knee MRIs. In this task, one must reconstruct a fully-sampled knee MRI image given a budget of only 25% of the  $\kappa$ -space measurements, where each  $\kappa$ -space measurement is a vertical line of width 1 pixel. We compare with existing MRI acceleration methods focused specifically on learning sampling strategies, namely PG-MRI (Bakker et al., 2020), LOUPE (Bahadir et al., 2020), and SeqMRI (Yin et al., 2021), each of which are detailed in Appendix A.6. We use the same data train / validation / test split and data preprocessing as Yin et al. (2021) for comparability. In particular, the data samples are  $\kappa$ -space slices cropped and centered at  $128 \times 128$ , with 34, 732 train samples, 1, 785 validation samples, and 1, 851 test samples. We train a DDIM on complex-valued image space samples  $\mathbf{x} \in \mathbb{C}^{128 \times 128}$  obtained by computing the inverse Fourier transform of the  $\kappa$ -space training samples (see Appendix A.2.2 for further training details). The data space is therefore the complex image space, with  $\kappa$ -space acting as the measurement space. This yields the measurement model  $\mathbf{y}_t = \mathbf{U}(A_t)\mathcal{F}(\mathbf{x}) + \mathbf{n}_t$ , where  $\mathcal{F}$  is the Discrete Fourier Transform,  $\mathbf{n}_t \sim \mathcal{N}_{\mathbb{C}}(0, \sigma_{\mathbf{y}}^2)$  is complex Gaussian measurement noise, and  $\mathbf{U}(A_t)$  is the subsampling matrix selecting samples at indices  $\in A_t$ . ADS proceeds by running Diffusion Posterior Sampling in the complex image domain with guidance from  $\kappa$ -space measurements through the measurement model, selecting maximum entropy lines in the  $\kappa$ -space. We observed on data from the validation set that ADS reconstruction performance increases with the number of reverse diffusion steps, although with diminishing returns for as steps increased. This indicates that in applying ADS, one can choose to increase sample quality at the cost of inference time and compute. To showcase the potential for ADS, we chose a large number of steps,  $T = 10k$ . Further, we choose guidance weight  $\zeta = 0.85$ , and sampling schedule  $S$  evenly partitioning  $[50, 2500]$ , and an initial action set  $A_{\text{init}} = \{63\}$ , starting with a single central  $\kappa$ -space line. Reconstructions are evaluated using the structural similarity index measure (SSIM) (Wang et al., 2004) to compare the absolute values of the fully-sampled target image and reconstructed image. The SSIM uses a window size of  $7 \times 7$  with  $k_1 = 0.01$  and  $k_2 = 0.03$  as set be the fastMRI challenge. Table 2 shows the SSIM results on the test set, comparing ADS to recent supervised methods, along with a fixed-mask Diffusion Posterior Sampling using the same inference parameters to serve as a strong unsupervised baseline. The fixed-mask used with DPS measures the 8% of lines at the center of the  $\kappa$ -space, and random lines elsewhere, as used by Zbontar et al. (2018). It is clear from the results that ADS using performs competitively with supervised baselines, and outperforms the fixed-mask diffusion-based approach. Figure 5 shows two reconstructions created by ADS. See Appendix A.7 for a histogram of all SSIMs over the test set for the diffusion-based approaches.

## 6 Discussion

While ADS appears to outperform fixed-mask baselines on both MNIST and fastMRI, it is interesting to note that the relative improvement offered by ADS differs significantly between datasets. For



Unsupervised	Method	SSIM ( $\uparrow$ )
$\times$	PG-MRI (Bakker et al., 2020)	87.97
$\times$	LOUPE (Bahadir et al., 2020)	89.52
$\checkmark$	Fixed-mask DPS	90.13
$\times$	SeqMRI (Yin et al., 2021)	91.08
$\checkmark$	ADS (Ours)	91.26

Table 2: SSIM scores for fastMRI knee test set with 4x acceleration. See Appendix A.7 for SSIM histograms for diffusion-based methods.

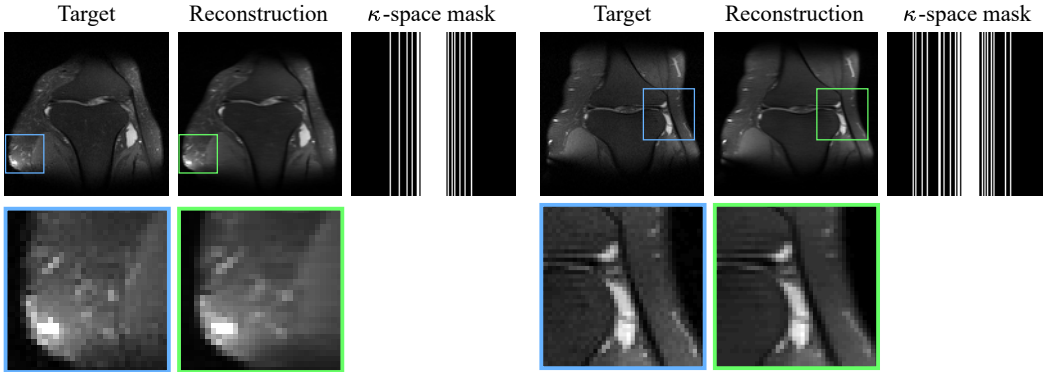


Figure 5: Sample fastMRI reconstructions produced by ADS, including the generated  $\kappa$ -space masks. The SSIMs are 95.8 for the left, and 94.4 for the right.

line-based image subsampling on MNIST with 25% samples, ADS achieves a 50% reduction in reconstruction error versus a fixed-mask approach (MAE = 0.019 vs 0.037), whereas with line-based  $\kappa$ -space subsampling for fastMRI with 25% samples, ADS achieves only a 12% relative improvement (SSIM = 91.26 vs 90.13). We find that the size of this performance gap between fixed and active mask design strategies can be explained by examining the distribution of masks designed by ADS on each task (See Appendix A.4). Indeed, the masks designed for fastMRI are very similar, whereas those designed for MNIST typically differ depending on the sample. When mask designs are similar, then fixed masks will perform similarly to actively designed masks. This is in part a feature of the data distribution – for example, most information in  $\kappa$ -space is contained in the center. Tasks in which one might expect significantly better performance from ADS are therefore those in which optimal masks will be highly sample-dependent.

In conclusion, we have proposed a method for using diffusion models as active subsampling agents without the need for additional training, using a simple, interpretable action selection policy. We show that this method significantly outperforms fixed-mask baselines on MNIST, and competes with existing supervised approaches in MRI acceleration without tasks-specific training. This method therefore takes a step towards transparent active sensing with automatically generated adaptive strategies, decreasing cost factors such as exposure time, and energy usage.

## 7 Limitations & Future Work

While experiments in Section 5 evidence some strengths of ADS against baseline sampling strategies, it is not without limitations. For example, the duration of inference in ADS is dependent on that of the diffusion posterior sampling method. Since low latency is essential in active subsampling, future work could aim to accelerate posterior sampling with diffusion models, leading to accelerated ADS. Another limitation is that the number of measurements taken is upper-bounded by the number of reverse diffusion steps  $T$ ; this limitation could be overcome by extending ADS to generate *batch designs* (Azimi et al., 2010), containing multiple measurements, from a single posterior estimate. Future work applying ADS in diverse domains would also help to further assess the robustness of the method.

## References

- B. D. Anderson. Reverse-time diffusion equation models. *Stochastic Processes and their Applications*, 12(3):313–326, 1982.
- J. Azimi, A. Fern, and X. Fern. Batch bayesian optimization via simulation matching. *Advances in neural information processing systems*, 23, 2010.
- C. D. Bahadir, A. Q. Wang, A. V. Dalca, and M. R. Sabuncu. Deep-learning-based optimization of the under-sampling pattern in mri. *IEEE Transactions on Computational Imaging*, 6:1139–1152, 2020.
- T. Bakker, H. van Hoof, and M. Welling. Experimental design for mri by greedy policy search. *Advances in Neural Information Processing Systems*, 33:18954–18966, 2020.
- L. Baldassarre, Y.-H. Li, J. Scarlett, B. Gözcü, I. Bogunovic, and V. Cevher. Learning-based compressive subsampling. *IEEE Journal of Selected Topics in Signal Processing*, 10(4):809–822, 2016.
- J. Bradbury, R. Frostig, P. Hawkins, M. J. Johnson, C. Leary, D. Maclaurin, G. Necula, A. Paszke, J. VanderPlas, S. Wanderman-Milne, and Q. Zhang. JAX: composable transformations of Python+NumPy programs, 2018. URL <http://github.com/google/jax>.
- G. Braun, S. Pokutta, and Y. Xie. Info-greedy sequential adaptive compressed sensing. *IEEE Journal of selected topics in signal processing*, 9(4):601–611, 2015.
- R. Bridson. Fast poisson disk sampling in arbitrary dimensions. *SIGGRAPH sketches*, 10(1):1, 2007.
- A. Caticha. Entropy, information, and the updating of probabilities. *Entropy*, 23(7):895, 2021.
- F. Chollet et al. Keras. <https://keras.io>, 2015.
- H. Chung and J. C. Ye. Score-based diffusion models for accelerated mri. *Medical image analysis*, 80:102479, 2022.
- H. Chung, J. Kim, M. T. Mccann, M. L. Klasky, and J. C. Ye. Diffusion posterior sampling for general noisy inverse problems. *arXiv preprint arXiv:2209.14687*, 2022.
- P. Dhariwal and A. Nichol. Diffusion models beat gans on image synthesis. In M. Ranzato, A. Beygelzimer, Y. Dauphin, P. Liang, and J. W. Vaughan, editors, *Advances in Neural Information Processing Systems*, volume 34, pages 8780–8794. Curran Associates, Inc., 2021. URL [https://proceedings.neurips.cc/paper\\_files/paper/2021/file/49ad23d1ec9fa4bd8d77d02681df5cfa-Paper.pdf](https://proceedings.neurips.cc/paper_files/paper/2021/file/49ad23d1ec9fa4bd8d77d02681df5cfa-Paper.pdf).
- D. Golovin and A. Krause. Adaptive submodularity: Theory and applications in active learning and stochastic optimization. *Journal of Artificial Intelligence Research*, 42:427–486, 2011.
- J. R. Hershey and P. A. Olsen. Approximating the kullback leibler divergence between gaussian mixture models. In *2007 IEEE International Conference on Acoustics, Speech and Signal Processing-ICASSP'07*, volume 4, pages IV–317. IEEE, 2007.
- J. Ho, A. Jain, and P. Abbeel. Denoising diffusion probabilistic models. *Advances in neural information processing systems*, 33:6840–6851, 2020.
- N. Houlsby, F. Huszár, Z. Ghahramani, and M. Lengyel. Bayesian active learning for classification and preference learning. *arXiv preprint arXiv:1112.5745*, 2011.
- I. Huijben, B. S. Veeling, and R. J. van Sloun. Deep probabilistic subsampling for task-adaptive compressed sensing. In *8th International Conference on Learning Representations, ICLR 2020*, 2020.
- Y. LeCun, L. Bottou, Y. Bengio, and P. Haffner. Gradient-based learning applied to document recognition. *Proceedings of the IEEE*, 86(11):2278–2324, 1998.
- D. V. Lindley. On a measure of the information provided by an experiment. *The Annals of Mathematical Statistics*, 27(4):986–1005, 1956.

- I. Loshchilov and F. Hutter. Fixing weight decay regularization in adam. *CoRR*, abs/1711.05101, 2017. URL <http://arxiv.org/abs/1711.05101>.
- M. Lustig and J. M. Pauly. Spirit: iterative self-consistent parallel imaging reconstruction from arbitrary k-space. *Magnetic resonance in medicine*, 64(2):457–471, 2010.
- T. Rainforth, A. Foster, D. R. Ivanova, and F. Bickford Smith. Modern bayesian experimental design. *Statistical Science*, 39(1):100–114, 2024.
- M. Rani, S. B. Dhok, and R. B. Deshmukh. A systematic review of compressive sensing: Concepts, implementations and applications. *IEEE access*, 6:4875–4894, 2018.
- R. Rombach, A. Blattmann, D. Lorenz, P. Esser, and B. Ommer. High-resolution image synthesis with latent diffusion models. In *Proceedings of the IEEE/CVF conference on computer vision and pattern recognition*, pages 10684–10695, 2022.
- L. Rout, Y. Chen, A. Kumar, C. Caramanis, S. Shakkottai, and W.-S. Chu. Beyond first-order tweedie: Solving inverse problems using latent diffusion, 2023.
- L. Rout, N. Raoof, G. Daras, C. Caramanis, A. Dimakis, and S. Shakkottai. Solving linear inverse problems provably via posterior sampling with latent diffusion models. *Advances in Neural Information Processing Systems*, 36, 2024.
- T. Sanchez, I. Krawczuk, Z. Sun, and V. Cevher. Closed loop deep bayesian inversion: Uncertainty driven acquisition for fast {mri}, 2020. URL <https://openreview.net/forum?id=BJ1P01BKDB>.
- J. Song, C. Meng, and S. Ermon. Denoising diffusion implicit models. *arXiv preprint arXiv:2010.02502*, 2020a.
- J. Song, A. Vahdat, M. Mardani, and J. Kautz. Pseudoinverse-guided diffusion models for inverse problems. In *International Conference on Learning Representations*, 2023. URL [https://openreview.net/forum?id=9\\_gsMA8MRKQ](https://openreview.net/forum?id=9_gsMA8MRKQ).
- Y. Song, J. Sohl-Dickstein, D. P. Kingma, A. Kumar, S. Ermon, and B. Poole. Score-based generative modeling through stochastic differential equations. *arXiv preprint arXiv:2011.13456*, 2020b.
- T. S. Stevens, N. Chennakeshava, F. J. de Bruijn, M. Pekař, and R. J. van Sloun. Accelerated intravascular ultrasound imaging using deep reinforcement learning. In *ICASSP 2022-2022 IEEE International Conference on Acoustics, Speech and Signal Processing (ICASSP)*, pages 1216–1220. IEEE, 2022.
- T. S. Stevens, F. C. Meral, J. Yu, I. Z. Apostolakis, J.-L. Robert, and R. J. Van Sloun. Dehazing ultrasound using diffusion models. *IEEE Transactions on Medical Imaging*, 2024.
- H. Van Gorp, I. Huijben, B. S. Veeling, N. Pezzotti, and R. J. Van Sloun. Active deep probabilistic subsampling. In *International Conference on Machine Learning*, pages 10509–10518. PMLR, 2021.
- Z. Wang, A. C. Bovik, H. R. Sheikh, and E. P. Simoncelli. Image quality assessment: from error visibility to structural similarity. *IEEE transactions on image processing*, 13(4):600–612, 2004.
- T. Yin, Z. Wu, H. Sun, A. V. Dalca, Y. Yue, and K. L. Bouman. End-to-end sequential sampling and reconstruction for mri. In *Machine Learning for Health*, pages 261–281. PMLR, 2021.
- P. Yu, S. Xie, X. Ma, B. Jia, B. Pang, R. Gao, Y. Zhu, S.-C. Zhu, and Y. N. Wu. Latent diffusion energy-based model for interpretable text modelling. In *International Conference on Machine Learning*, pages 25702–25720. PMLR, 2022.
- J. Zbontar, F. Knoll, A. Sriram, T. Murrell, Z. Huang, M. J. Muckley, A. Defazio, R. Stern, P. Johnson, M. Bruno, et al. fastmri: An open dataset and benchmarks for accelerated mri. *arXiv preprint arXiv:1811.08839*, 2018.

## A Appendix / supplemental material

### A.1 Derivation of Equation (10)

Here we show that maximising the policy function does not require computing a set of particles for each possible action in the case where the action is a subsampling mask. Because the subsampling mask  $A_t = A_{t-1} \cup a_t$  only varies in  $a_t$  in the arg max, the elements of each particle  $\hat{\mathbf{y}}^{(i)}$  will remain the same for each possible  $A_t$  except for at those indices selected by  $a_t$ . We therefore decompose the squared L2 norm into two squared L2 norms, one for the indices in  $a_t$  and the other for those in  $A_{t-1}$ . The latter then becomes a constant in the argmax, and can be ignored. This results in a formulation in which we only need to compute the squared L2 norms for the set of elements corresponding with  $a_t$ . We use  $\mathbf{U}(A_t)$  to indicate the subsampling matrix containing 1s on the diagonal at indices in  $A_t$ .

$$\begin{aligned}
a_t^* &= \arg \max_{a_t} \sum_i^{N_p} \log \sum_j^{N_p} \exp \left\{ \frac{\|\hat{\mathbf{y}}_t^{(i)} - \hat{\mathbf{y}}_t^{(j)}\|_2^2}{2\sigma_y^2} \right\} \\
&= \arg \max_{a_t} \sum_i^{N_p} \log \sum_j^{N_p} \exp \left\{ \frac{\|\mathbf{U}(A_t)f(\hat{\mathbf{x}}_0^{(i)}) - \mathbf{U}(A_t)f(\hat{\mathbf{x}}_0^{(j)})\|_2^2}{2\sigma_y^2} \right\} \\
&= \arg \max_{a_t} \sum_i^{N_p} \log \sum_j^{N_p} \exp \left\{ \frac{\sum_{k \in A_t} (f(\hat{\mathbf{x}}_0^{(i)})_k - f(\hat{\mathbf{x}}_0^{(j)})_k)^2}{2\sigma_y^2} \right\} \\
&= \arg \max_{a_t} \sum_i^{N_p} \log \sum_j^{N_p} \exp \left\{ \frac{\sum_{l \in a_t} (f(\hat{\mathbf{x}}_0^{(i)})_l - f(\hat{\mathbf{x}}_0^{(j)})_l)^2 + \sum_{m \in A_{t-1}} (f(\hat{\mathbf{x}}_0^{(i)})_m - f(\hat{\mathbf{x}}_0^{(j)})_m)^2}{2\sigma_y^2} \right\} \\
&= \arg \max_{a_t} \sum_i^{N_p} \log \sum_j^{N_p} \left( \exp \left\{ \frac{\sum_{l \in a_t} (f(\hat{\mathbf{x}}_0^{(i)})_l - f(\hat{\mathbf{x}}_0^{(j)})_l)^2}{2\sigma_y^2} \right\} \exp \left\{ \frac{\sum_{m \in A_{t-1}} (f(\hat{\mathbf{x}}_0^{(i)})_m - f(\hat{\mathbf{x}}_0^{(j)})_m)^2}{2\sigma_y^2} \right\} \right) \\
&= \arg \max_{a_t} \sum_i^{N_p} \log \sum_j^{N_p} \exp \left\{ \frac{\sum_{l \in a_t} (f(\hat{\mathbf{x}}_0^{(i)})_l - f(\hat{\mathbf{x}}_0^{(j)})_l)^2}{2\sigma_y^2} \right\} \\
&= \arg \max_{a_t} \sum_i^{N_p} \log \sum_j^{N_p} \exp \left\{ \frac{\sum_{l \in a_t} (\hat{\mathbf{y}}_l^{(i)} - \hat{\mathbf{y}}_l^{(j)})^2}{2\sigma_y^2} \right\}
\end{aligned} \tag{12}$$

### A.2 Training Details

The methods and models are implemented in the Keras 3.1 (Chollet et al., 2015) library using the Jax backend (Bradbury et al., 2018).

#### A.2.1 MNIST DDIM Training Details

The model is trained using one GeForce RTX 2080 Ti (NVIDIA, Santa Clara, CA, USA) with 11 GB of VRAM. The training run of 500 epochs took one hours to complete on the specified GPU.

The DDIM architecture is provided by Keras3 at the following URL: <https://keras.io/examples/generative/ddim/>. We use widths=[32, 64, 128], block\_depth=2, diffusion\_steps=30, ema\_0.999, learning\_rate=0.0001, weight\_decay=0.0001, loss="mae".

#### A.2.2 FastMRI DDIM Training Details

This section provides training details for the training of the DDIM model on FastMRI.

Most of the training details are given in Section 5.2. Additionally, to train the DDIM model, we use the AdamW optimizer (Loshchilov and Hutter, 2017) with an empirically chosen learning rate  $1 \times 10^{-4}$ . The model is trained using one GeForce RTX 2080 Ti (NVIDIA, Santa Clara, CA, USA) with 11 GB of VRAM. The other hyperparameters were not tuned and therefore the model was trained only once. The training run of 305 epochs took 28 hours to complete on the specified GPU.

The DDIM architecture is provided by Keras3 at the following URL: <https://keras.io/examples/generative/ddim/>. We use `widths=[32, 64, 96, 128]`, `block_depth=2`, `diffusion_steps=30`, `ema_0.999`, `learning_rate=0.0001`, `weight_decay=0.0001`, `loss="mae"`.

### **A.3 Validation details**

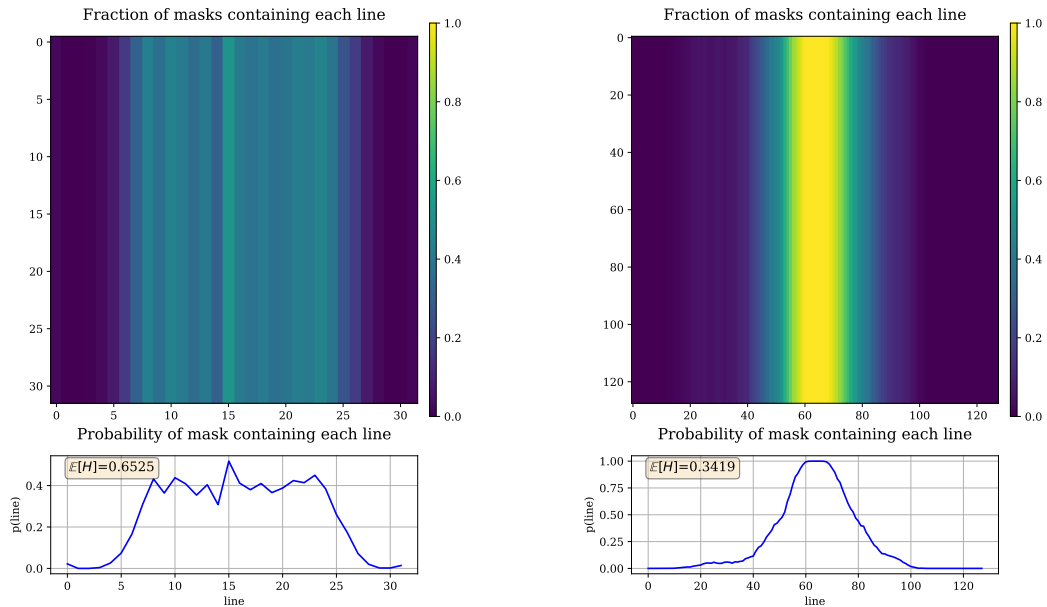
#### **A.3.1 Evaluating FastMRI subsampling strategies**

To evaluate the subsampling strategies we utilized a cloud compute cluster with job scheduler. The compute cluster utilizes A100 GPUs (NVIDIA, Santa Clara, CA, USA). This allowed us to parallelize the execution of the diffusion model accross multiple GPUs. For the subsampling strategies some minor hyperparameter tuning was done. To evaluate the complete test set sequentially on one A100 GPU takes 30 hours. other than the hyperparameter tuning there were no other (failed) experiments that used compute.

#### **A.3.2 Evaluating MNIST subsampling strategies**

The MNIST experiments used 22 GPU hours on a GeForce RTX 2080 Ti (NVIDIA, Santa Clara, CA, USA) with 11 GB of VRAM. Every diffusion step takes 5 ms. For 1000 diffusion steps, 3 methods, 500 test samples and 11 sampling rates this equals 22 hours. See Figure ?? for an example of ADS on MNIST.

#### A.4 ADS Mask Distributions for MNIST and fastMRI



(a) ADS mask distribution for 500 samples from the MNIST test set.

(b) ADS mask distribution for 1851 samples from the fastMRI test set.

Figure 6: The distribution of masks chosen by ADS varies according to the task. We observe that the masks chosen for MNIST are less predictable a priori than those chosen for fastMRI, leading to a stronger performance by ADS relative to fixed-mask approaches. We plot at the bottom of each plot estimates of the probability that each line will appear in a mask generated by ADS as Bernoulli variables (either the line is present in the mask, or not). To quantify the predictability of these masks, we compute the average entropy over each of these variables, finding that MNIST masks are significantly less predictable than those for fastMRI.

### A.5 ADS with latent diffusion models

Using a pretrained Stable Diffusion model, ADS is tested on Imagenet (Figure 9), CelebA (Figure 7), FFHQ (Figure 10). Stable Diffusion is run for 1000 steps, with 400 ms per step for each example shown here.

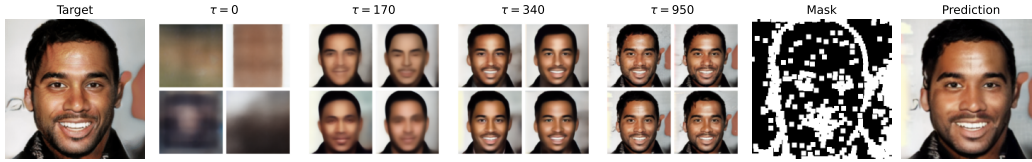


Figure 7: Example of ADS inference on the CelebA dataset.

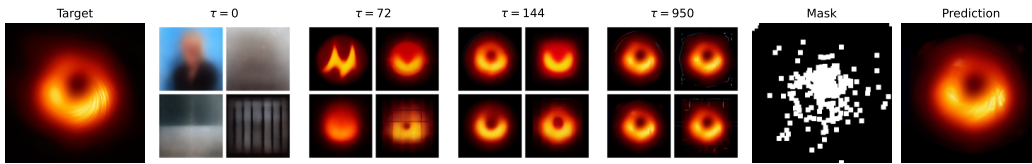


Figure 8: Example of ADS inference on the black hole image.

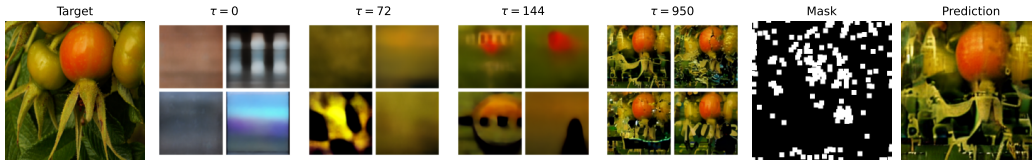


Figure 9: Example of ADS inference on the Imagenet dataset.



Figure 10: Example of ADS inference on the FFHQ dataset.

## A.6 FastMRI Comparison Methods

### A.6.1 PG-MRI

Bakker et al. (2020) use policy-gradient methods from Reinforcement Learning to learn a policy function  $\pi_\phi(a_t | \hat{x}_t)$  that outputs new measurement locations given the current reconstruction. Reconstructions are then generated using a pre-existing U-Net based reconstruction model provided by the fastMRI repository.

### A.6.2 LOUPE

LOUPE (Bahadir et al., 2020) introduces a end-to-end learning framework that trains a neural network to output under-sampling masks in combination with an anti-aliasing (reconstruction) model on undersampled full-resolution MRI scans. Their loss function consists of a reconstruction term and a trick to enable sampling a mask.

### A.6.3 SeqMRI

With SeqMRI, Yin et al. (2021) propose an end-to-end differentiable sequential sampling framework. They therefore jointly learn the sampling policy and reconstruction, such that the sampling policy can best fit with the strengths and weaknesses of the reconstruction model, and vice versa.

## A.7 FastMRI SSIM Distributions

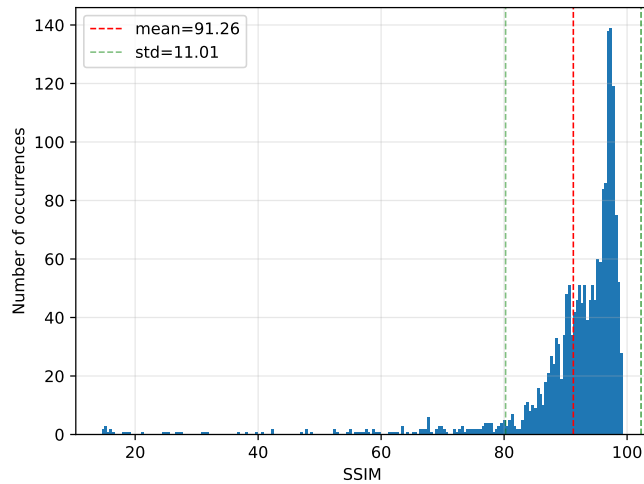


Figure 11: 200-bin histogram showing distribution of SSIM scores across the FastMRI knee test set for 4x acceleration using ADS.



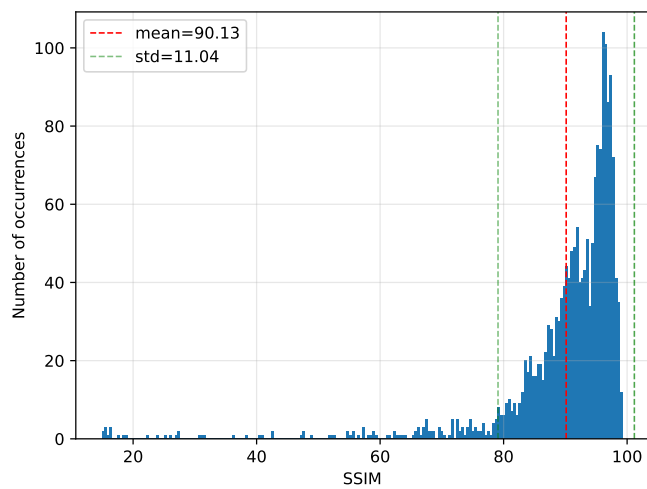


Figure 12: 200-bin histogram showing distribution of ssim scores across the FastMRI knee test set for 4x acceleration using diffusion posterior sampling with fixed  $\kappa$ -space masks.